Earth and Planetary Science Letters 510 (2019) 45–52

Contents lists available at ScienceDirect

Earth and Planetary Science Letters

www.elsevier.com/locate/epsl

Melting curve of iron to 290 GPa determined in a resistance-heated diamond-anvil cell

Ryosuke Sinmyo [a,b,*], Kei Hirose [a,b], Yasuo Ohishi [c]

[a] Earth-Life Science Institute, Tokyo Institute of Technology, 2-12-1 Ookayama, Meguro, Tokyo 152-8550, Japan
[b] Department of Earth and Planetary Science, Graduate School of Science, The University of Tokyo, 7-3-1 Hongo, Bunkyo, Tokyo 113-0033, Japan
[c] Japan Synchrotron Radiation Research Institute, 1-1-1 Koto, Sayo, Hyogo 679-5198, Japan

ARTICLE INFO

Article history:
Received 12 June 2018
Received in revised form 9 December 2018
Accepted 4 January 2019
Available online xxxx
Editor: J. Brodholt

Keywords:
core
iron
melting
high pressure
inner core boundary
core–mantle boundary

ABSTRACT

The Earth's core is composed mainly of iron. Since the liquid core coexists with solid at the inner core boundary (ICB), the melting point of iron at 330 GPa offers a key constraint on core temperatures. However, previous results using a laser-heated diamond-anvil cell (DAC) have been largely inconsistent with each other, likely because of an intrinsic large temperature gradient and its temporal fluctuation. Here we employed an internal-resistance-heated DAC and determined the melting temperature of pure iron up to 290 GPa, for the first time above 200 GPa by static compression experiments. A small extrapolation of the present experimental results yields a melting point of 5500 ± 220 K at the ICB, higher than 4850 ± 200 K reported by previous laser-heated DAC by Boehler (1993) but is lower than 6230 ± 500 K by Anzellini et al. (2013). Accounting for the melting temperature depression due to core-alloying elements, the upper bounds for the temperature at the ICB and the core–mantle boundary (CMB) are estimated to be 5120 ± 390 K and 3760 ± 290 K, respectively. Such low present-day CMB temperature suggests that the lowermost mantle has avoided global melting, at least since early Proterozoic Eon.

1. Introduction

Since the melting curve of iron constrains the temperatures of planetary cores, a number of studies have attempted to determine the melting temperature of iron under high pressures. A pioneering ultrahigh-pressure laser-heated DAC experiment performed by Boehler (1993) reported the melting temperature of iron up to 200 GPa, in which melting was judged visually as the onset of convective motion. Extrapolation of his melting curve gives the melting point of iron to be 4850 ± 200 K at 330 GPa corresponding to the pressure at ICB. The melting curve of iron has then been repeatedly examined by laser-heated DAC studies (Ma et al., 2004; Shen et al., 2004; Anzellini et al., 2013; Aquilanti et al., 2015; Zhang et al., 2016), but the results have been markedly different from each other. While Shen et al. (2004) reported, on the basis of diffuse x-ray scattering from liquid, a relatively low melting curve close to Boehler (1993)'s, Anzellini et al. (2013) using the same melting criterion obtained the highest melting temperature among all previous DAC results. Anzellini and others found the melting point of iron to be 6230 ± 500 K at 330 GPa by extrapolating their results from 200 GPa, which is approximately consistent with shock compression data (Brown and McQueen, 1986; Williams et al., 1987; Yoo et al., 1993; Nguyen and Holmes, 2004) and theoretical calculations (Alfè, 2009; Sola and Alfè, 2009) except Laio et al. (2000). The two most recent DAC works based on x-ray absorption spectroscopy (Aquilanti et al., 2015) and synchrotron Mössbauer spectroscopy (Zhang et al., 2016), however, again demonstrated iron melting curves significantly lower than Anzellini et al. (2013)'s. These conflicting results are likely due to large spatial and temporal temperature variations, especially in the direction parallel to the compressional axis, in a laser-heated DAC samples. Another source of the discrepancy may be the difference in melting criterion employed by each previous study. Furthermore, the previous DAC experiments were carried out only up to 200 GPa and thus required long extrapolation to 330 GPa, which is another source of large uncertainty.

Here we employed internal-resistance-heated DAC techniques, which stabilize sample temperature during heating compared to conventional laser heating (Fig. 1, Supplementary Movie 1). Experiments were carried out up to 290 GPa and 5360 K, far beyond the pressure and temperature (P–T) range ever achieved in earlier

* Corresponding author at: Department of Earth and Planetary Science, Graduate School of Science, The University of Tokyo, 7-3-1 Hongo, Bunkyo, Tokyo 113-0033, Japan.
E-mail address: sinmyo@eps.s.u-tokyo.ac.jp (R. Sinmyo).

https://doi.org/10.1016/j.epsl.2019.01.006
0012-821X/

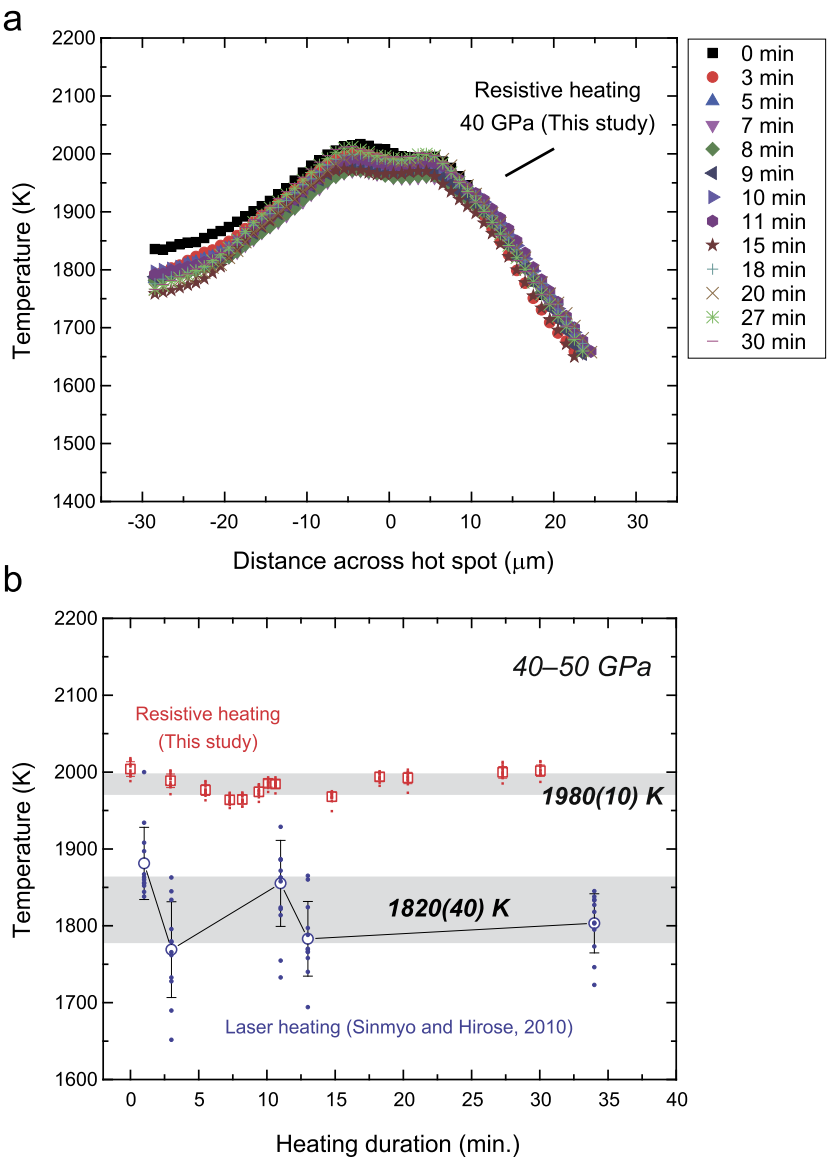

Fig. 1. Temperature stability and homogeneity in an internal-resistance-heated DAC. (a) Change in temperature profile across a hot spot in 30 min. (b) Comparison of temperature stability and variation in 15 μm area between laser-heated (Sinmyo and Hirose, 2010) and internal-resistance-heated DAC samples.

internal-resistance-heated DAC studies (<100 GPa, <2000 K) (Zha et al., 2008; Komabayashi et al., 2012). The melting temperature of iron was determined on the basis of the change in voltage–temperature relation to 290 GPa, close to the pressure at the ICB.

2. Experimental methods

2.1. Internal-resistance-heated DAC experiments

High-pressure melting experiments were conducted using an internal-resistance-heated DAC (Fig. 2a). Beveled or flat diamond anvils with 60–300 μm culet size were used. We employed a composite (inner cubic BN and outer Re) gasket that was electrically insulated. Pure iron foil with a thickness of 1 μm was fabricated with a focused ion beam (FIB) system (FEI Versa 3D DualBeam); the central part of the foil was narrowed in order to locate a hot spot and generate temperature high enough to melt iron. Note that we used a thin sample foil in order to 1) enhance electrical resistivity and 2) reduce axial temperature variation (see below), although the thin sample did not provide a diffuse x-ray signal when melted. The foil was loaded between the Al_2O_3 thermal insulation layers and connected to an electrode several millimeters away from the culet. To avoid moisture on the sample, the whole DAC assembly was dried after loading in a vacuum oven at 423 K for more than 12 hrs. When the oven was opened, dry argon was introduced, and the sample was compressed in an Ar atmosphere. After compression to a desired pressure, direct electrical current was applied to the iron foil for heating. DC current was supplied by using a power source (Takasago ZX-400) under the voltage-control mode with a stability within ±0.1% in volt. Ramp rates were typically several hundred millivolt per second. One-dimensional temperature profile was obtained parallel to the view given in Fig. 2a by a spectroradiometric method (Ohishi et al., 2008) (Fig. 1). We adjusted the temperature measurement position to the hottest part of a sample with <1 μm precision.

Pressures were obtained on the basis of the equations of state of face-centered-cubic (fcc) and hexagonal-close-packed (hcp) Fe (Dewaele et al., 2006; Tsujino et al., 2013) when x-ray diffraction (XRD) data were available (Table 1). In runs without XRD measurements, we determined the pressure at 300 K after heating from the Raman peak shift of the culet of a diamond anvil (Akahama and Kawamura, 2006) and corrected for a thermal pressure contri-

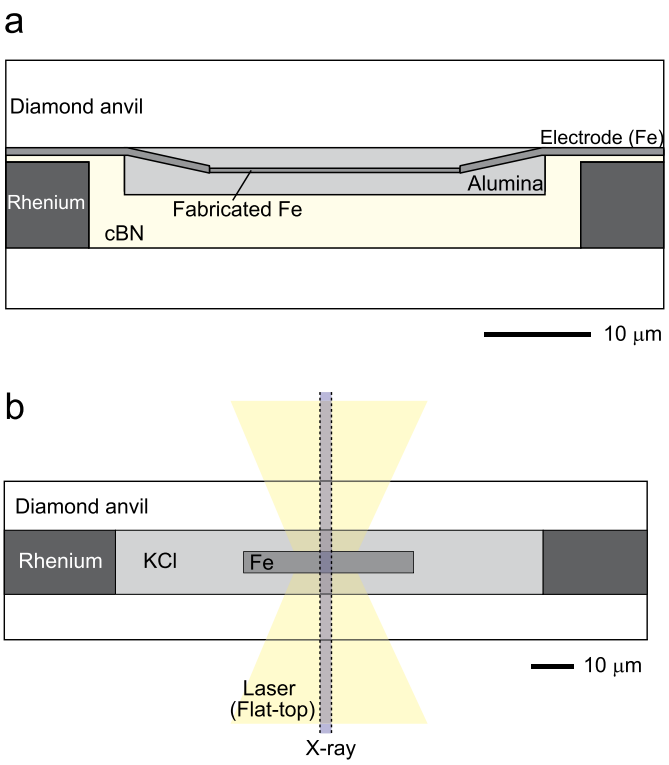

Fig. 2. Sample configurations for internal-resistance-heated and laser-heated DAC experiments. Sample dimensions in an internal-resistance-heated DAC (a) are from the present FIB/SEM analyses on the sample recovered from ~97 GPa (Fig. 3a). Sample thickness and the sizes of laser and x-ray beams for a laser-heated DAC experiment (b) at ~90 GPa are from Anzellini et al. (2013).

Table 1
Results of melting experiments.

Run #	P (GPa)	T_{melt} (K)	Solid phase at T_{melt}
1	6(1)	1900(100)	not analyzed
2	57(6)	2620(130)	not analyzed
3	67(3)	2760(140)	fcc
4	94(9)	3030(150)	not analyzed
5	97(5)	3030(150)	fcc
6	129(6)	3210(160)	hcp
7	134(7)	3470(170)	hcp
8	151(8)	3610(180)	hcp
9	154(8)	3570(180)	hcp
10	155(8)	3610(180)	hcp
11	211(11)	4250(210)	hcp
12	216(11)	4440(220)	hcp
13	230(12)	4780(240)	hcp
14	244(12)	4660(230)	hcp
15	257(13)	5000(250)	hcp
16	285(14)	5120(260)	hcp
17	290(15)	5360(270)	hcp

Numbers in parentheses indicate uncertainty in the last digits.

bution as +0.004 GPa/K, which was estimated by the present XRD measurements at similar pressure range (run #3).

2.2. XRD measurements and chemical analyses

Synchrotron XRD measurements were conducted at BL10XU, SPring-8 (Ohishi et al., 2008). A monochromatic x-ray beam with a wavelength of 0.413–0.415 Å was collimated to 6 μm at full width of half maximum (FWHM) in runs performed below ~150 GPa and to 2 μm at higher pressures. Angle-dispersive XRD patterns were collected on a flat panel detector (PerkinElmer XRD 0822) with typical exposure time of 1 sec.

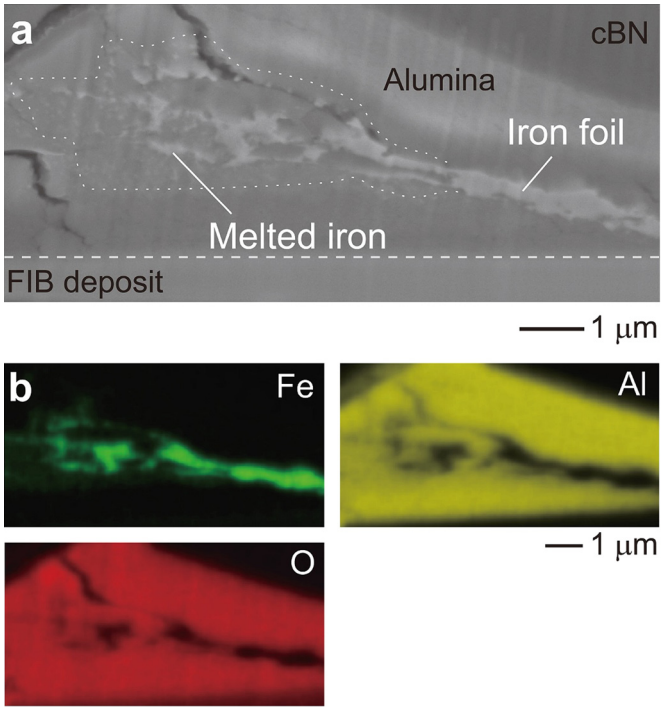

Fig. 3. Sample texture after melting. (a) Back-scattered electron image of the iron sample recovered from 97 GPa and 3030 K. (b) X-ray maps of iron, aluminum, and oxygen for the area same as (a). The sample was not contaminated by oxygen nor carbon.

After sample was recovered from a DAC, its cross section – parallel to the compressional axis and perpendicular to the view in Fig. 2a – was prepared by an FIB. It was then examined for texture and composition (Fig. 3) with a field-emission-type scanning electron microscope (FE-SEM) and an energy dispersive x-ray spectroscopy (EDS) operated at 10 kV and 0.17 nA in the dual-beam FIB system. Results of chemical analyses showed that contamination by oxygen or aluminum were not found in the iron sample (Fig. 3b). A very weak carbon peak was detected from any part of a sample chamber including alumina and unheated area. After subtracting higher background in the EDS spectrum for the iron sample, which was caused by continuous x-rays that arise when high energy electrons approach the nucleus of a heavy metal, the amounts of carbon found in iron and surrounding alumina were similar to each other, indicating that carbon was contaminated during EDS analysis. Moreover, they were also similar between quenched molten iron and unmelted solid iron, which also supports that the contamination took place not during high-pressure experiment because otherwise carbon should be enriched in liquid several times more than in solid (Morard et al., 2017). Additionally, it is noted that even if a very minor amount of carbon was present during heating and induced melting at low temperatures by eutectic melting, the fraction of liquid should have been small, considering the Fe–C eutectic liquid composition at relevant pressure (Fei and Brosh, 2014).

3. Results

3.1. Melting criterion

We obtained the voltage–temperature relationship for the iron sample during heating by applying electricity (Fig. 4). Sample temperature increased with increasing applied voltage; however, after reaching a certain temperature, the temperature started fluctuating. At the same time, we observed anomaly in the voltage–resistance curve (Fig. 5). In addition, the voltage–resistance relation

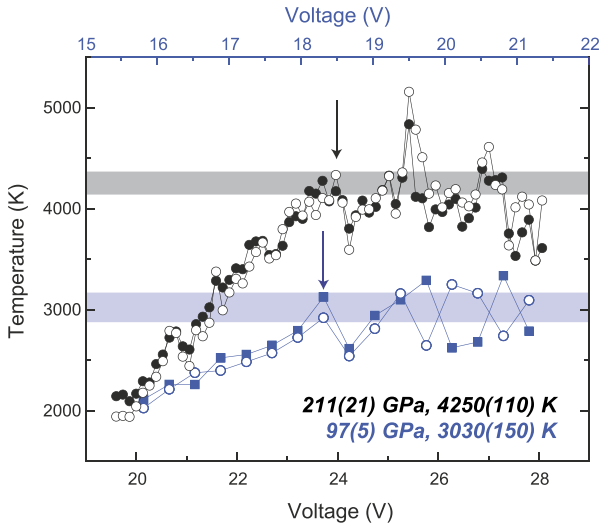

Fig. 4. The onset of melting inferred from applied voltage–sample temperature relation. Data are from runs #5 at ~97 GPa (blue) and #11 at ~211 GPa (black). Both filled and open symbols show temperatures at two different areas next to each other. The sample temperature started to fluctuate after reaching a melting point (arrows). (For interpretation of the colors in the figure(s), the reader is referred to the web version of this article.)

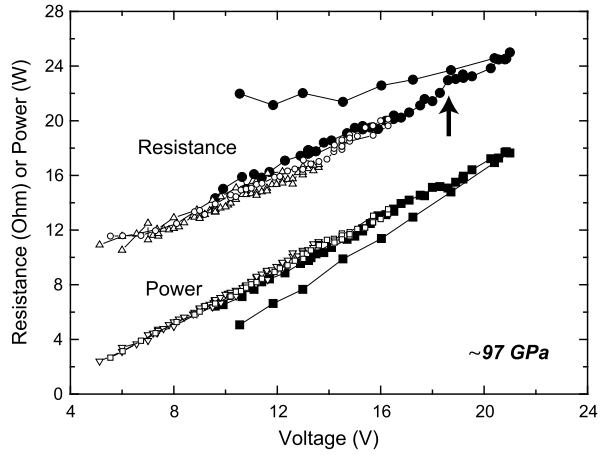

Fig. 5. Changes in electrical resistance and power with changing applied voltage in an internal-resistance-heated DAC at ~97 GPa. Open and closed symbols are the data obtained in run #5 from heating cycles heated below and beyond melting point, respectively. Arrow indicates the onset of melting shown in Fig. 4. The voltage–resistance relation during temperature increase was well reproduced during temperature decrease unless sample melted. In contrast, melting of the sample changed the voltage–resistance relation.

became no longer identical during temperature increase and decrease (note the same voltage–resistance path during increasing and decreasing voltage unless such temperature fluctuation occurred at some point).

Both of such temperature fluctuation (Fig. 4) and change in the voltage–resistance relationship (Fig. 5) are attributed to a morphology change upon melting. Textural observation of a sample cross section indicated that thickness of an unmelted part of the sample was similar from cold to hot regions next to a molten area. It suggests that the deformation of solid iron was not significant even right below melting temperature, and therefore not responsible for the observed change in electrical resistance. As described above, microprobe analyses on recovered samples performed after melting experiments showed no contamination by carbon, oxygen, or aluminum in the iron sample (Fig. 3b). These show that the onset of fluctuation in the voltage–temperature relation can be used as a melting criterion (Fig. 4). While it was stable at constant voltage

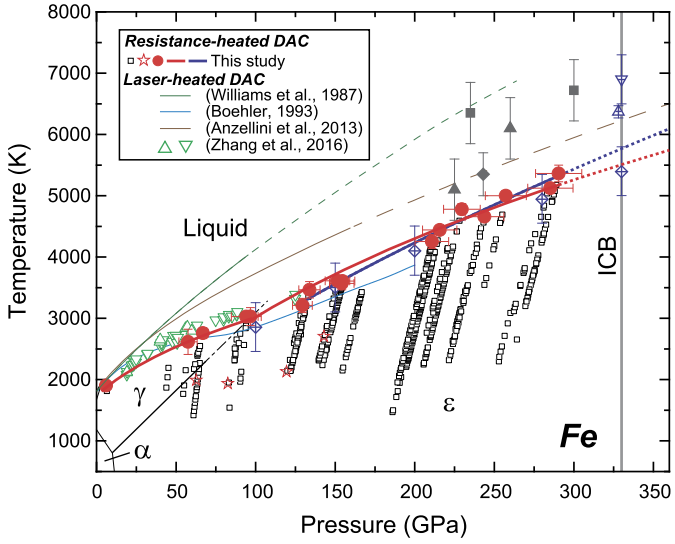

Fig. 6. The melting curve of iron. Red curve = this study (black open squares, before melting; red closed circles, onset of melting). Blue curve = alternative fitting result using an equation proposed by Simon and Glatzel (1929). Fast recrystallization (stars) was observed at temperatures much lower than the melting curve. Previous DAC experiments; green (Williams et al., 1987), blue (Boehler, 1993), and brown curves (Anzellini et al., 2013), and green normal and inverse triangles (Zhang et al., 2016) for Fe and $Fe_{0.9}Ni_{0.1}$, respectively. Theoretical predictions; blue diamonds (Laio et al., 2000), triangle (Alfè, 2009), and inverse triangle (Sola and Alfè, 2009). Shock-wave data; filled diamond (Brown and McQueen, 1986), filled squares (Yoo et al., 1993), and filled triangles (Nguyen and Holmes, 2004). The γ–ε boundary is from a previous internal-resistance-heated DAC study (α, bcc; γ, fcc; ε, hcp iron) (Komabayashi et al., 2009).

(Fig. 1), temperature slightly fluctuated during increasing the voltage (Fig. 4). Considering such fluctuations, we set ±5% uncertainty in melting temperature determined in the present experiments (Table 1).

3.2. Melting curve of iron

Seventeen separate runs were performed between 6 and 290 GPa to determine the melting temperature of iron (Table 1, Fig. 6) on the basis of the applied voltage–sample temperature relation (Fig. 4). In run #5, when we heated hcp Fe, the fcc phase appeared above 2770 K at 92 GPa (Fig. 7), consistent with the earlier experiments on the fcc–hcp boundary (Komabayashi et al., 2009). The XRD peaks of fcc then diminished with further temperature increase to 3030 K, which coincides with the onset of sample temperature fluctuation (Fig. 4). After high P–T experiment, we recovered this sample from the DAC and observed a clear melting texture in its cross section (Fig. 3a). The melting temperature of iron should therefore be 3030 ± 150 K at 97 GPa. Even at higher pressures, we successfully observed the onset of fluctuation in the voltage–temperature relation (Fig. 4) and obtained the melting point of iron to 290 GPa, well above the pressure range examined in previous DAC studies (<200 GPa) (Boehler, 1993; Shen et al., 2004; Anzellini et al., 2013; Aquilanti et al., 2015; Zhang et al., 2016).

We have tested the reproducibility of the present melting temperature determination by conducting three separate experiments at 151, 154, and 155 GPa. The melting temperatures obtained were 3610(±40), 3570(±100), and 3610(±20) K, respectively, all in excellent agreement with each other. When XRD data were collected continuously during heating, fast appearance/disappearance of diffraction spots, so called “fast recrystallization,” was observed at temperatures much lower than melting points (Fig. 6).

The melting temperatures found at 129 to 290 GPa where hcp is stable at melting point were fitted by the equation pro-

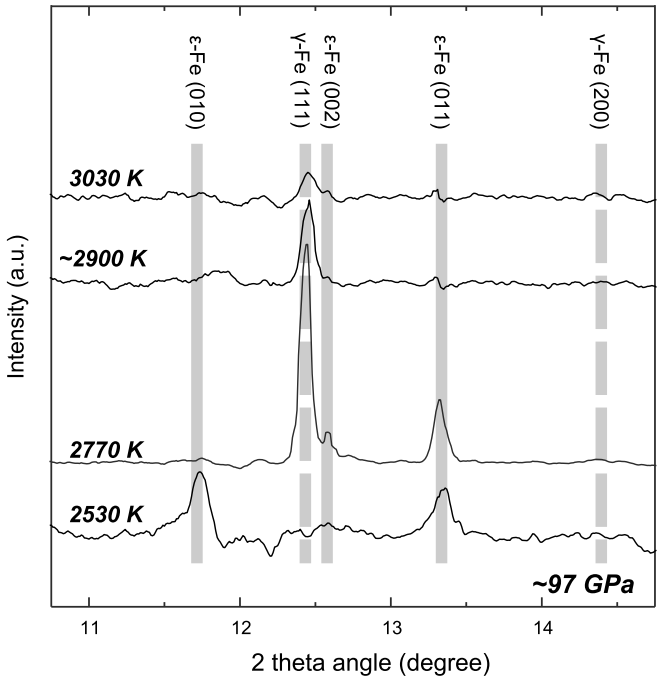

Fig. 7. Changes in x-ray diffraction pattern with increasing temperature at ~97 GPa (run #5). Each represents XRD pattern after subtracting the profile collected during melting in order to highlight the changes in peaks from solid iron. γ–Fe, fcc iron; ε–Fe, hcp iron. Fcc iron appeared above 2770 K, consistent with previous internal-resistance-heated DAC study (Komabayashi et al., 2009). It vanished at 3030 K at which melting was recognized in the voltage–temperature relation (Fig. 4). Intensity scale is the same for all spectra.

posed by Kraut and Kennedy (1966) (Fig. 6); $T_{\rm melt}/T_{\rm ref} = [1 + 3.10(\pm 0.12) \times (V_{\rm ref} - V)/V]$, in which $T_{\rm ref}$ and $V_{\rm ref}$ are reference temperature (2996 K) and volume (16.823 Å^3 corresponding to 98.5 GPa) at liquid–hcp–fcc triple point (Boehler, 1993; Komabayashi et al., 2009; Zhang et al., 2016). The location of the triple point reported in these previous studies is consistent with the present XRD measurements describe above (Fig. 7). A small extrapolation of our melting curve gives 5500 ±220 K at 330 GPa (Fig. 6). Errors in melting temperature here indicate 95% confidence band of the fitting with weighting pressure. When we employ a classical equation by Simon and Glatzel (1929) for fitting, we obtain the melting temperature of 5770 ± 280 K at 330 GPa (Fig. 6).

Additionally, the present XRD measurements demonstrated that iron was in hcp structure at melting points above 129 GPa, while earlier experiment and theory have suggested a phase transformation from hcp to fcc (Mikhaylushkin et al., 2007) or to body-centered-cubic (bcc) (Belonoshko et al., 2017) with increasing temperature. Belonoshko and others predicted that at 360 GPa hcp and bcc iron are stable at 6000 and 7000 K, respectively, but our data indicate that hcp iron melts at 5740 K before any transformation to bcc (Fig. 6).

4. Discussion

4.1. Comparison with previous studies

The melting temperature determined to be 3030 ± 150 K at 97 GPa (run #5, see above for details) agrees with those reported by recent x-ray absorption (Aquilanti et al., 2015) and Mössbauer spectroscopy studies (Zhang et al., 2016), but 600 K lower than that by Anzellini et al. (2013) based on the appearance of a diffuse x-ray signal at equivalent pressure (Fig. 6). The present estimates of 5500 ± 220 K at the ICB pressure is higher than 4850 ± 200 K reported by Boehler (1993) but is lower than 6230 ± 500 K obtained by the extrapolation of Anzellini et al.'s melting data. Melting temperatures obtained by previous shock experiments are higher than our results based on a resistance-heated DAC. This may be due to the overestimation of temperature in shock compression data (Boehler, 2000).

The difference between the melting curves determined by Anzellini et al. (2013) and this study can be partly attributed to the difference in sample temperature distribution in laser-heated and internal-resistance-heated DACs employed in these studies, respectively. We have calculated thermal structures in these DAC samples in Fig. 8. Sample dimensions employed here correspond to those around 90 GPa, where 1) the difference between the melting temperatures of iron obtained by using these two techniques is large (Anzellini et al., 2013; this study) and 2) the morphology of our sample (run #5) was examined by an electron microscope (Fig. 3a). According to Anzellini et al. (2013), total thickness of Fe + KCl layers was ~15 μm under pressures up to 90 GPa, in which iron portion may have been 1/3 (Fig. 2b). They also described that a laser beam was focused to 5–20 μm (FWHM). Since the beam shape was not mentioned, we considered an ideal flat-top beam intensity distribution with a diameter of 15 μm. The thermal conductivities of Fe (Konopkova et al., 2016; Ohta et al., 2016), Al_2O_3, KCl, and Re were from literature (Haynes, 2016). Our model showed slightly larger temperature variations in a laser-heated DAC sample than the previous study by Rainey et al. (2013), in which the thermal parameter of platinum (Terada et al., 2005) was used. Platinum exhibits higher thermal conductivity than iron at high P–T, which is likely the source of the different temperature gradient. The calculated temperature distribution shows that the center of the iron sample is lower by as much as 250 K (Fig. 8a) when the surface temperature is ~3600 K at the hot spot. Such temperature difference between the sample surface and the inside is larger if we employ the thermal conductivity of liquid iron that is lower than that of solid (Ohta et al., 2016), while it can be smaller if liquid state convection occurs. It is noted that the absorbance of a laser beam was assumed to be homogeneous but could be variable in both space and time because it is sensitive to sample surface conditions such as roughness and reflectivity. Indeed, the sample temperature in a laser-heated DAC was less stable than in an internal-resistance-heated DAC (Fig. 1b).

For an internal-resistance-heated DAC sample, we employed the sample configuration found in run #5 heated at ~97 GPa (Fig. 2a), in which 0.4 μm thick iron foil was sandwiched by 2 μm thick Al_2O_3 layers as observed in an SEM image (Fig. 3a). We ignored cBN, because it was away from the hot spot. Moreover, cBN has high thermal conductivity and was in contact with a diamond anvil, and thus it can be regarded as a part of the diamond anvil in the thermal modeling. The sample was electrically heated homogeneously from the surface to the center, but heat was lost from the surface. Therefore, the center should have been hotter by 80 K at ~3600 K (Fig. 8b).

When a diffuse x-ray signal was observed, it is likely that not only the surface but also the inside of the sample was molten. It leads to an overestimation of melting temperature because the temperature was measured at the surface. If this is the case, Anzellini et al. (2013) may have overestimated the melting temperature by as much as 250 K. On the other hand, our internal-resistance-heated DAC experiments could underestimate the melting temperature by 80 K. Overall, more than half of the mismatch between the melting temperatures obtained by laser- and resistance-heated DAC experiments may be reconciled with the difference in the sample thickness in addition to the heating technique. Indeed, axial temperature variations can be smaller in a laser-heated DAC sample when it is thinner. In this case, however, it will be difficult to observe an x-ray diffuse signal. On the con-

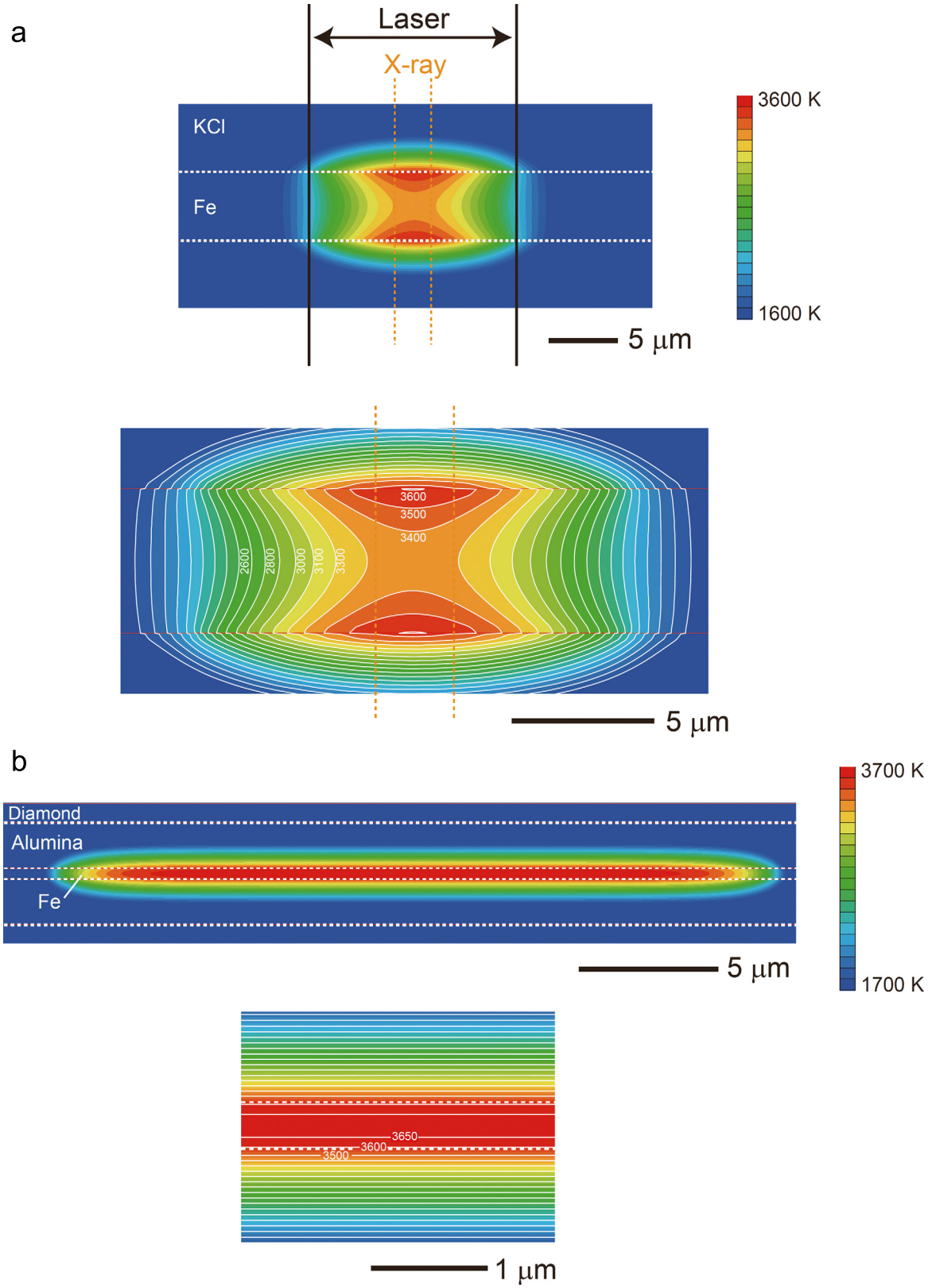

Fig. 8. Temperature distribution around iron sample simulated by finite elements modeling. Sample dimensions and configuration in a laser-heated DAC (a) are from Anzellini et al. (2013) for ~90 GPa. Temperature measured at sample surface is hotter by as much as 250 K than at the center. Those for an internal-resistance-heated DAC (b) referred to run #5 performed at ~97 GPa (Fig. 3a). The surface of the sample is colder by 80 K than at the center.

trary, the change in voltage–temperature relationship employed in this study is a reasonable melting criterion applicable to a very thin sample.

The appearance of diffuse x-ray scattering is the direct evidence for melting but difficult to see at high pressure because it requires a sufficient volume of liquid. Anzellini et al. (2013) employed a relatively thick sample but were able to observe a diffuse signal only up to 150 GPa, less than half of the pressure at the ICB, likely because the sample became too thin at higher pressures. Instead of trying to obtain the diffuse scattering signal from a thick sample, we used a thin foil as a sample (0.4 μm thick at 97 GPa, see Fig. 3a), which enhanced electrical resistance and enabled high-temperature generation and melting of iron to 290 GPa at 5360 ± 140 K. Note also that the thin sample foil employed in this study helped reduce axial temperature variation remarkably, as discussed above. Quick appearance and disappearance of diffraction spots, so called "fast recrystallization", were observed in this study at temperatures lower than those reported in previous DAC experiments (Boehler et al., 2008; Anzellini et al., 2013). Indeed, the interpretation of this phenomenon is still under debate; while it could be due to the reorientation of crystals in a partially melted sample (Boehler et al., 2008), it was observed at temperatures lower than melting temperatures (Anzellini et al., 2013). The different results may be due to the difference in the definition of fast recrystallization. In this study, we define it as the appearance and disappearance of at least one diffraction spot in two-dimensional XRD image obtained every 1 sec.

4.2. Implications for the present-day core temperature

The melting point of pure iron, 5500 ± 220 K at 330 GPa (Fig. 6), gives the upper limit for the temperature at ICB, since the liquid outer core includes light elements that depress melting temperature. Such effect depends on impurity elements; −30(±30) K/wt% Si (Morard et al., 2014), −90(±30) K/wt% O, −150(±90) K/wt% S, and −470(±340) K/wt% C at CMB pressure (Morard et al., 2014, 2017) and −450 K/wt% H at 15 GPa (Shibazaki et al., 2014). Considering their maximum concentrations theoretically calculated to account for the outer core density deficit – 7 wt% Si, 5 wt% O, 9 wt% S, 4 wt% C (Badro et al., 2014), and 1.0 wt% H (Badro et al., 2014; Umemoto and Hirose, 2015) – the depression is estimated to be −210(±210) K by Si, −450(±150) K by O and H, −1350(±810) K by S, and −1880(±1360) K by C if the outer core contains a single light element. These values were estimated assuming that the liquidus temperature is depressed linearly with increasing the concentration of each light element (Morard et al., 2017). The minimum depression is found when core contains 7 wt% Si, but it is not likely because eutectic liquid in the Fe–FeSi binary includes less than 2 wt% Si and thus liquid Fe with >2 wt% Si crystallizes CsCl-type Fe–Si alloy being more enriched in silicon than liquid (Ozawa et al., 2016). The Fe–FeSi subsolidus phase relations obtained by Fischer et al. (2012) are not consistent with those by Ozawa et al. (2016) likely because of a kinetic effect due to slow diffusion of silicon in solid iron, but the melting experiments in the latter should have suffered minimal kinetic problem. The combination of 2 wt% Si and 3.6 wt% O (or 0.7 wt% H) indeed gives the least depression of the outer core liquidus temperature by 380(±170) K, although an Fe–Si–O liquid core is also unlikely (Hirose et al., 2017). Therefore, the ICB temperature should be lower than 5120 ± 390 K.

These also give the upper bound for the temperature at CMB to be 3760 ± 290 K by employing the outer core density profile and the Grüneisen parameter $\gamma = 1.5$ (Vočadlo et al., 2003). Here we consider the adiabatic temperature profile without stratification. It is certainly lower than the dry solidus temperature of ∼4150 K for a pyrolitic/chondritic mantle at the CMB (Fiquet et al., 2010; Andrault et al., 2011), consistent with the fact that the bottom of the mantle is now not molten globally. On the other hand, ultra-low velocity zones (ULVZs) may indicate the presence of partial melts locally above the CMB. Our data suggest that the temperature at the CMB can be higher than the solidus temperature of a basaltic material (3800 ± 150 K) (Andrault et al., 2014), supporting the argument that subducted basaltic crust partially melts and causes the ULVZs. Alternatively, it is also possible that the partial melts were originally formed when the mantle was hotter and have evolved by fractional crystallization to compositions close to FeO (Boukare et al., 2015; Kato et al., 2016), whose melting temperature is 3690 K at the bottom of the mantle (Fischer and Campbell, 2010).

The traditional estimate of the present-day CMB temperature is about 4000 K (Boehler, 1993; Anzellini et al., 2013), marginally less than the dry solidus temperature (∼4150 K) of a pyrolitic/chondritic mantle (Fiquet et al., 2010; Andrault et al., 2011). The recent core energetics modeling by Hirose et al. (2017) demonstrated that maintaining a geodynamo with 1 TW ohmic dissipation requires the core cooling rate as low as 100 K/Gyr when we consider SiO_2 crystallization at the CMB, while it should have been much higher if core convection has been driven by thermal buoyancy rather than compositional buoyancy (Labrosse, 2015). Therefore, if the current CMB temperature is ≥4000 K, the minimum core cooling rate 100 K/Gyr leads to global melting of the lowermost mantle at least 1.5 Gyr ago. If this is the case, when crustal materials subducted down to the bottom of the mantle more than 1.5 Gyr ago, they are likely to have interacted with silicate melts above the CMB. As a consequence of chemical reaction with the melts at the bottom of the mantle, the crustal materials should have lost or modified their original geochemical signatures before being involved in mantle upwellings and recycled to the surface. However, recycled crustal materials older than 1.5 Gyr are widely observed in the sources of ocean island basalts (Kimura et al., 2016). Moreover, Polynesian plumes involve recycled oceanic crust material with a mass-independent sulfur isotopic anomaly that was formed exclusively by atmospheric photochemical reactions more than 2.45 Gyr ago (Cabral et al., 2013). These support that the CMB temperature is, at least lower than 4000 K at present, consistent with the relatively low melting temperature of iron found in this study.

Acknowledgements

We thank J. Kimura and T. Iizuka for valuable discussions on the recycling of slab materials. K. Yonemitsu helped FIB/EDS analysis. This work was supported by JSPS Kakenhi grant JP16H06023, JP16H01115, and JP16H06285. Two anonymous reviewers are acknowledged for their thoughtful and constructive comments.

Appendix A. Supplementary material

Supplementary material related to this article can be found online at https://doi.org/10.1016/j.epsl.2019.01.006.

References

Akahama, Y., Kawamura, H., 2006. Pressure calibration of diamond anvil Raman gauge to 310 GPa. J. Appl. Phys. 100, 043516.

Alfè, D., 2009. Temperature of the inner-core boundary of the Earth: melting of iron at high pressure from first-principles coexistence simulations. Phys. Rev. B 79, 060101(R).

Andrault, D., Bolfan-Casanova, N., Lo Nigro, G., Bouhifd, M.A., Garbarino, G., Mezouar, M., 2011. Solidus and liquidus profiles of chondritic mantle: implication for melting of the Earth across its history. Earth Planet. Sci. Lett. 304, 251–259.

Andrault, D., Pesce, G., Bouhifd, M.A., Bolfan-Casanova, N., Henot, J.-M., Mezouar, M., 2014. Melting of subducted basalt at the core–mantle boundary. Science 344, 892–895.

Anzellini, S., Dewaele, A., Mezouar, M., Loubeyre, P., Morard, G., 2013. Melting of iron at Earth's inner core boundary based on fast X-ray diffraction. Science 340, 464–466.

Aquilanti, G., Trapananti, A., Karandikar, A., Kantor, I., Marini, C., Mathon, O., Pascarelli, S., Boehler, R., 2015. Melting of iron determined by X-ray absorption spectroscopy to 100 GPa. Proc. Natl. Acad. Sci. USA 112, 12042–12045.

Badro, J., Cote, A.S., Brodholt, J.P., 2014. A seismologically consistent compositional model of Earth's core. Proc. Natl. Acad. Sci. USA 111, 7542–7545.

Belonoshko, A.B., Lukinov, T., Fu, J., Zhao, J., Davis, S., Simak, S.I., 2017. Stabilization of body-centred cubic iron under inner-core conditions. Nat. Geosci. 10, 312–316.

Boehler, R., 1993. Temperatures in the Earth's core from melting-point measurements of iron at high static pressures. Nature 363, 534–536.

Boehler, R., 2000. High-pressure experiments and the phase diagram of lower mantle and core materials. Rev. Geophys. 38, 221–245.

Boehler, R., Santamaria-Perez, D., Errandonea, D., Mezouar, M., 2008. Melting, density, and anisotropy of iron at core conditions: new X-ray measurements to 150 GPa. J. Phys. Conf. Ser. 121, 022018.

Boukaré, C.E., Ricard, Y., Fiquet, G., 2015. Thermodynamics of the MgO–FeO–SiO_2 system up to 140 GPa: application to the crystallization of Earth's magma ocean. J. Geophys. Res. 120, 6085–6101.

Brown, J.M., McQueen, R.G., 1986. Phase transitions, Grüneisen parameter, and elasticity for shocked iron between 77 GPa and 400 GPa. J. Geophys. Res. 91, 7485–7494.

Cabral, R.A., Jackson, M.G., Rose-Koga, E.F., Koga, K.T., Whitehouse, M.J., Antonelli, M.A., Farquhar, J., Day, J.M., Hauri, E.H., 2013. Anomalous sulphur isotopes in plume lavas reveal deep mantle storage of Archaean crust. Nature 496, 490–493.

Dewaele, A., Loubeyre, P., Occelli, F., Mezouar, M., Dorogokupets, P.I., Torrent, M., 2006. Quasihydrostatic equation of state of iron above 2 Mbar. Phys. Rev. Lett. 97, 215504.

Fei, Y., Brosh, E., 2014. Experimental study and thermodynamic calculations of phase relations in the Fe–C system at high pressure. Earth Planet. Sci. Lett. 408, 155–162.

Fiquet, G., Auzende, A.L., Siebert, J., Corgne, A., Bureau, H., Ozawa, H., Garbarino, G., 2010. Melting of peridotite to 140 gigapascals. Science 329, 1516–1518.

Fischer, R.A., Campbell, A.J., 2010. High-pressure melting of wüstite. Am. Mineral. 95, 1473–1477.

Fischer, R.A., Campbell, A.J., Caracas, R., Reaman, D.M., Dera, P., Prakapenka, V.B., 2012. Equation of state and phase diagram of Fe–^{16}Si alloy as a candidate component of Earth's core. Earth Planet. Sci. Lett. 357, 268–276.

Haynes, W.M., 2016. CRC Handbook of Chemistry and Physics. CRC Press, Boca Raton.

Hirose, K., Morard, G., Sinmyo, R., Umemoto, K., Hernlund, J., Helffrich, G., Labrosse, S., 2017. Crystallization of silicon dioxide and compositional evolution of the Earth's core. Nature 543, 99–102.

Kato, C., Hirose, K., Nomura, R., Ballmer, M.D., Miyake, A., Ohishi, Y., 2016. Melting in the FeO–SiO_2 system to deep lower-mantle pressures: implications for subducted banded iron formations. Earth Planet. Sci. Lett. 440, 56–61.

Kimura, J.I., Gill, J.B., Skora, S., van Keken, P.E., Kawabata, H., 2016. Origin of geochemical mantle components: role of subduction filter. Geochem. Geophys. Geosyst. 17, 3289–3325.

Komabayashi, T., Fei, Y., Meng, Y., Prakapenka, V., 2009. In-situ X-ray diffraction measurements of the gamma–epsilon transition boundary of iron in an internally-heated diamond anvil cell. Earth Planet. Sci. Lett. 282, 252–257.

Komabayashi, T., Hirose, K., Ohishi, Y., 2012. In situ X-ray diffraction measurements of the fcc–hcp phase transition boundary of an Fe–Ni alloy in an internally heated diamond anvil cell. Phys. Chem. Miner. 39, 329–338.

Konopkova, Z., McWilliams, R.S., Gomez-Perez, N., Goncharov, A.F., 2016. Direct measurement of thermal conductivity in solid iron at planetary core conditions. Nature 534, 99–101.

Kraut, E.A., Kennedy, G.C., 1966. New melting law at high pressures. Phys. Rev. 151, 608–609.

Labrosse, S., 2015. Thermal evolution of the core with a high thermal conductivity. Phys. Earth Planet. Inter. 247, 36–55.

Laio, A., Bernard, S., Chiarotti, G.L., Scandolo, S., Tosatti, E., 2000. Physics of iron at Earth's core conditions. Science 287, 1027–1030.

Ma, Y.Z., Somayazulu, M., Shen, G.Y., Mao, H.K., Shu, J.F., Hemley, R.J., 2004. In situ X-ray diffraction studies of iron to Earth-core conditions. Phys. Earth Planet. Inter. 143, 455–467.

Mikhaylushkin, A.S., Simak, S.I., Dubrovinsky, L., Dubrovinskaia, N., Johansson, B., Abrikosov, I.A., 2007. Pure iron compressed and heated to extreme conditions. Phys. Rev. Lett. 99, 165505.

Morard, G., Andrault, D., Antonangeli, D., Bouchet, J., 2014. Properties of iron alloys under the Earth's core conditions. C. R. Géosci. 346, 130–139.

Morard, G., Andrault, D., Antonangeli, D., Nakajima, Y., Auzende, A., Boulard, E., Cervera, S., Clark, A., Lord, O., Siebert, J., 2017. Fe–FeO and Fe–Fe_3C melting relations at Earth's core–mantle boundary conditions: implications for a volatile-rich or oxygen-rich core. Earth Planet. Sci. Lett. 473, 94–103.

Nguyen, J.H., Holmes, N.C., 2004. Melting of iron at the physical conditions of the Earth's core. Nature 427, 339–342.

Ohishi, Y., Hirao, N., Sata, N., Hirose, K., Takata, M., 2008. Highly intense monochromatic X-ray diffraction facility for high-pressure research at SPring-8. High Press. Res. 28, 163–173.

Ohta, K., Kuwayama, Y., Hirose, K., Shimizu, K., Ohishi, Y., 2016. Experimental determination of the electrical resistivity of iron at Earth's core conditions. Nature 534, 95–98.

Ozawa, H., Hirose, K., Yonemitsu, K., Ohishi, Y., 2016. High-pressure melting experiments on Fe–Si alloys and implications for silicon as a light element in the core. Earth Planet. Sci. Lett. 456, 47–54.

Rainey, E., Hernlund, J., Kavner, A., 2013. Temperature distributions in the laser-heated diamond anvil cell from 3-D numerical modeling. J. Appl. Phys. 114, 204905.

Shen, G.Y., Prakapenka, V.B., Rivers, M.L., Sutton, S.R., 2004. Structure of liquid iron at pressures up to 58 GPa. Phys. Rev. Lett. 92, 185701.

Shibazaki, Y., Terasaki, H., Ohtani, E., Tateyama, R., Nishida, K., Funakoshi, K., Higo, Y., 2014. High-pressure and high-temperature phase diagram for $Fe_{0.9}Ni_{0.1}$–H alloy. Phys. Earth Planet. Inter. 228, 192–201.

Simon, F., Glatzel, G., 1929. Bemerkungen zur Schmelzdruckkurve. Z. Anorg. Allg. Chem. 178, 309–316.

Sinmyo, R., Hirose, K., 2010. The Soret diffusion in laser-heated diamond-anvil cell. Phys. Earth Planet. Inter. 180, 172–178.

Sola, E., Alfè, D., 2009. Melting of iron under Earth's core conditions from diffusion Monte Carlo free energy calculations. Phys. Rev. Lett. 103, 078501.

Terada, Y., Ohkubo, K., Mohri, T., 2005. Thermal conductivities of platinum alloys at high temperatures. Platin. Met. Rev. 49, 21–26.

Tsujino, N., Nishihara, Y., Nakajima, Y., Takahashi, E., Funakoshi, K., Higo, Y., 2013. Equation of state of gamma–Fe: reference density for planetary cores. Earth Planet. Sci. Lett. 375, 244–253.

Umemoto, K., Hirose, K., 2015. Liquid iron–hydrogen alloys at outer core conditions by first-principles calculations. Geophys. Res. Lett. 42, 7513–7520.

Vočadlo, L., Alfe, D., Gillan, M., Price, G.D., 2003. The properties of iron under core conditions from first principles calculations. Phys. Earth Planet. Inter. 140, 101–125.

Williams, Q., Jeanloz, R., Bass, J., Svendsen, B., Ahrens, T.J., 1987. The melting curve of iron to 250 gigapascals: a constraint on the temperature at Earth's center. Science 236, 181–182.

Yoo, C.S., Holmes, N.C., Ross, M., Webb, D.J., Pike, C., 1993. Shock temperatures and melting of iron at Earth core conditions. Phys. Rev. Lett. 70, 3931–3934.

Zha, C.-S., Mibe, K., Bassett, W.A., Tschauner, O., Mao, H.-K., Hemley, R.J., 2008. P–V–T equation of state of platinum to 80 GPa and 1900 K from internal resistive heating/x-ray diffraction measurements. J. Appl. Phys. 103, 054908.

Zhang, D., Jackson, J.M., Zhao, J., Sturhahn, W., Alp, E.E., Hu, M.Y., Toellner, T.S., Murphy, C.A., Prakapenka, V.B., 2016. Temperature of Earth's core constrained from melting of Fe and $Fe_{0.9}Ni_{0.1}$ at high pressures. Earth Planet. Sci. Lett. 447, 72–83.